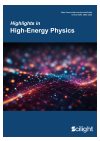
Scilight

Highlights in High-Energy Physics
https://www.sciltp.com/journals/hihep



Check for updates

Review

Di-Higgs Production at the Inverse-Attobarn Scale

Caterina Vernieri

SLAC National Accelerator Laboratory, 2575 Sand Hill Rd, Menlo Park, CA 94025, USA; caterina@slac.stanford.edu

How To Cite: Vernieri, C. Di-Higgs Production at the Inverse-Attobarn Scale. *Highlights in High-Energy Physics* **2026**, *2*(4), 12. https://doi.org/10.53941/hihep.2026.100012

Received: 16 August 2026
Revised: 6 October 2026
Accepted: 15 October 2026
Published: 6 November 2026

Abstract: Higgs boson pair production provides direct experimental access to the trilinear Higgs self-coupling and hence plays a central role in the energy frontier physics program. This paper presents the status of the searches for Di-Higgs production at the LHC as the field prepares for legacy analyses of the full Run 3 dataset. In the last decade, expected sensitivities have progressed from order-of-magnitude limits on the cross section to within reach of the Standard Model prediction. The first joint ATLAS and CMS combination, using Run 2 datasets of 126–140 fb^{-1} at 13 TeV, reaches an expected upper limit of 1.7 times the SM HH production rate in the absence of signal. The three most sensitive decay channels, $b\bar{b}\gamma\gamma$, $b\bar{b}\tau^{+}\tau^{-}$, and $b\bar{b}b\bar{b}$, are used to examine two developments behind this progress. The first is the increase in sensitivity enabled by machine-learning advances in reconstruction, triggering, and analysis techniques, beyond the gain expected from luminosity alone. The second is the growing impact of background and signal modeling, including theoretical uncertainties. Current searches remain statistically limited overall, but their dominant systematic uncertainties already reduce the sensitivity and will determine how effectively the larger LHC and HL-LHC datasets could be used.

Keywords: Higgs boson; Higgs boson pair production; Higgs self-coupling; electroweak symmetry breaking; hadron collider physics

1. Introduction

The discovery of the Higgs boson in 2012 [1,2] established the existence of a scalar field responsible for electroweak symmetry breaking. It also opened a new experimental program: determining whether the Higgs sector has the minimal form realized in the Standard Model (SM), or is the low-energy manifestation of a richer underlying dynamics. In the SM, electroweak symmetry breaking is realized through the Higgs doublet Φ and its scalar potential

$$V(\Phi) = -\mu^2\,\Phi^{\dagger}\Phi + \lambda\,(\Phi^{\dagger}\Phi)^2.$$

This is the simplest renormalizable form capable of generating a non-zero vacuum expectation value (v). The SM does not explain the origin of the potential, its parameters, or whether the Higgs field is the only scalar participating in electroweak symmetry breaking. Along the neutral scalar direction, the potential can be expanded around its minimum as $\phi = v + h$, where $v = 246$ GeV locates the electroweak minimum and h is the physical Higgs-field fluctuation. This gives the trilinear and quartic self-interactions

$$V(v+h) = V(v) + \tfrac{1}{2}m_H^2 h^2 + \lambda_3\, v\, h^3 + \tfrac{1}{4}\lambda_4 h^4, \qquad \lambda^{\mathrm{SM}} = \lambda_3 = \lambda_4 = \frac{m_H^2}{2v^2} \simeq 0.13. \tag{1}$$

The vacuum expectation value v fixes the location of the electroweak minimum, while the precisely measured Higgs mass fixes its curvature, $V''(v) = m_H^2$ [3,4]. Together they specify the SM potential, but its higher-order terms have not been measured directly. Measuring the trilinear self-coupling, λ, therefore provides the first direct test of the Higgs potential beyond this curvature. Deviations are expressed through the coupling modifier $\kappa_\lambda \equiv \lambda/\lambda^{\mathrm{SM}}$. A representative higher-dimensional deformation that preserves the location and curvature of the electroweak minimum is illustrated in Figure 1a.

Copyright: © 2026 by the authors. This is an open access article under the terms and conditions of the Creative Commons Attribution (CC BY) license (https://creativecommons.org/licenses/by/4.0/).
Publisher's Note: Scilight stays neutral with regard to jurisdictional claims in published maps and institutional affiliations.

Determining the shape of the Higgs potential experimentally is connected to several open problems in particle physics and cosmology. The Higgs sector may contain additional scalar states or provide a portal to dark matter. Such dynamics can modify the potential even when no new state is directly accessible and single-Higgs observables remain consistent with their SM predictions. Higgs boson pair production is directly sensitive to modifications of the Higgs self-interactions through the trilinear self-coupling. The Higgs potential also governs the electroweak phase transition: while the SM predicts a smooth crossover, new scalar interactions can induce a first-order transition, providing one of the necessary ingredients for electroweak baryogenesis. Likewise, conclusions about the stability of the electroweak vacuum rely on extrapolating the SM potential to very high energy scales under the assumption that no new physics modifies its evolution. A direct determination of the Higgs self-coupling is therefore not simply another precision test of the SM, but a qualitatively new probe of electroweak symmetry breaking [5–7].

At hadron colliders, λ is accessed directly through Higgs boson pair production. The dominant HH cross section, through gluon-fusion (ggF), is roughly three orders of magnitude below single-Higgs production, suppressed by destructive interference between the top-quark box diagram and the Higgs self-coupling triangle diagram (Figure 1b). The same interference provides the sensitivity to λ: varying κ_λ modifies both the inclusive cross section and the shape of the m_{HH} spectrum, particularly in the low-m_{HH} region. At the time of the 2019 community review [5], the combined expected limits stood at 10–13 times the SM rate, and observation was regarded as a goal for the High-Luminosity LHC (HL-LHC).

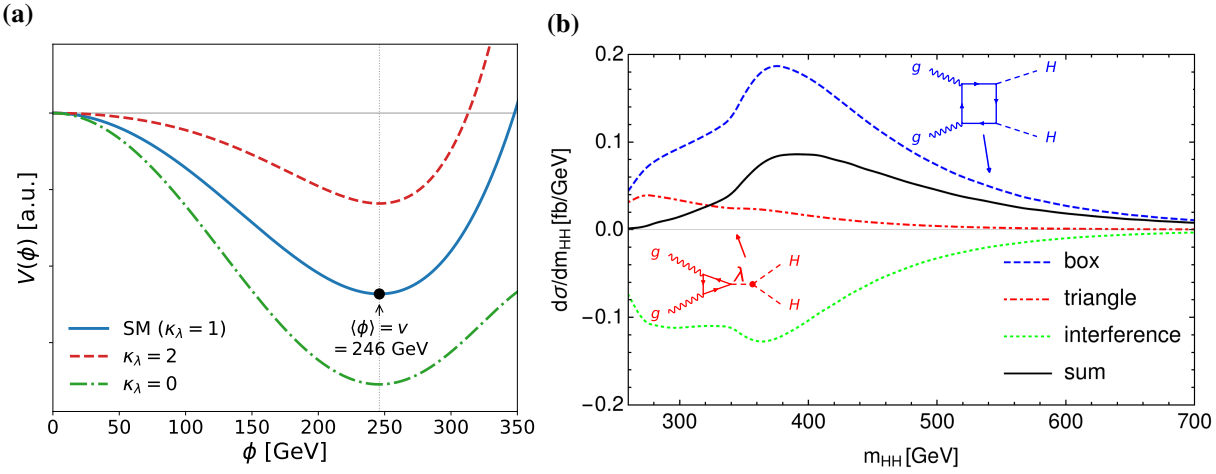


Figure 1. (**a**) Schematic deformations of the Higgs potential. All curves have an electroweak minimum at $v = 246$ GeV with the same curvature, $V''(v) = m_H^2$, while the trilinear and higher Higgs self-interactions vary in a correlated way. (**b**) Leading-order differential cross section as a function of m_{HH} for $gg \to HH$, decomposed into the box (blue dashed), triangle (red dashed), and interference (green dotted) contributions. The black solid curve shows their sum. Adapted from Ref. [5]. The trilinear coupling that modifies the potential around the minimum in (**a**) also enters the triangle topology in (**b**).

Seven years later, the first joint ATLAS + CMS combination of the full Run 2 datasets, corresponding to 126–140 fb^{-1} of pp collisions at 13 TeV per experiment, reports an HH signal strength $\mu_{HH} \equiv \sigma_{HH}/\sigma_{HH}^{\mathrm{SM}} = 0.8^{+0.9}_{-0.7}$ and an expected upper limit of 1.7 times the SM prediction [8]. This improvement is greater than expected from luminosity scaling alone. This review examines how advances in object reconstruction, triggering, and analysis methods, many based on machine learning, have contributed to this progress, and which systematic uncertainties will affect the sensitivity of the next results.

By the end of Run 3 in June 2026, ATLAS and CMS had each recorded approximately 0.5 ab^{-1} of pp collision data in total, including 332 and 327 fb^{-1}, respectively, at 13.6 TeV [9,10]. The available Run 3 sample therefore already exceeds Run 2 by more than a factor of two, while the current HH analyses use at most about half of this sample. The approved HL-LHC program, beginning with Run 4, will extend the dataset toward 3 ab^{-1} per experiment.

We restrict the discussion to non-resonant HH production. The remainder of this review is organized as follows. Section 2 summarizes the theory predictions used in the measurements. Section 3 reviews the Run 2 legacy through the three golden channels, $b\bar{b}\gamma\gamma$, $b\bar{b}\tau^+\tau^-$, and $b\bar{b}b\bar{b}$, and their combinations. Section 4 discusses machine-learning in reconstruction and triggering, while Section 5 examines how these and analysis-level developments enter the first Run 3 results. Section 6 introduces interpretations beyond one-parameter $\kappa_\lambda$scans, and Section 7 closes with the HL-LHC program and the future-collider landscape as framed by the 2026 European Strategy update [11].

2. Theory Predictions for Higgs Boson Pair Production

Alongside the experimental developments, theory predictions are an essential ingredient in the normalization and interpretation of the HH signal, through both the inclusive rate and the kinematic distributions used to determine κ_λ. For gluon fusion, the results reported here use the reference SM inclusive cross section adopted by ATLAS and CMS: $\sigma^{HH}_{\text{ggF}} = 30.8^{+2.0}_{-7.1}$ fb at $\sqrt{s} = 13$ TeV and $34.1^{+2.2}_{-7.9}$ fb at 13.6 TeV [12]. This prediction is based on the NNLO$_{\text{FTapprox}}$ QCD calculation, which combines the exact NLO calculation with full top-quark-mass dependence [13] with NNLO corrections evaluated in the heavy-top limit and improved by finite-mass reweighting [14]. The quoted uncertainty combines renormalization- and factorization-scale variations with variations of the renormalization scheme and scale of the top-quark mass, and also includes the PDF and α_s uncertainties [12, 15]. The ggF signal samples used in the principal analyses are generated at NLO with full top-quark mass dependence using the POWHEG `ggHH` implementation [16,17] and interfaced to parton showers. Beyond the dominant gluon-fusion process, Higgs boson pairs are also produced through vector-boson fusion (VBF) and, at smaller rates, in association with a vector boson (VHH) or a top-quark pair ($t\bar{t}HH$). The VBF cross-section normalization includes the N^{3}LO QCD prediction [18] and electroweak corrections [19]. The VHH and $t\bar{t}HH$ searches use NNLO and NLO signal predictions, respectively. The reference cross sections and the perturbative accuracy used for the principal HH production modes are summarized in Table 1.

Table 1. SM Higgs-pair production cross sections used in recent searches or provided by current LHC Higgs Working Group (LHCHWG) recommendations [20]; the VHH components are quoted separately for ZHH, W^+HH, and W^-HH. The first ggF entry quotes a total uncertainty including QCD-scale, top-quark mass renormalization scheme, and PDF+α_s contributions. For the 2026 entry, scale, numerical, and mass-scheme uncertainties are added linearly, and PDF+α_s is quoted separately. For VBF and VHH, the first and second quoted uncertainties arise from scale variation and PDFs, respectively. For $t\bar{t}HH$, they arise from scale variation and PDF+α_s, respectively. All uncertainties are quoted as relative percentages.

Production Mode	13 TeV [fb]	13.6 TeV [fb]	Main Theory Input
ggF HH	$30.8^{+6.5\%}_{-23.1\%}$	$34.1^{+6.5\%}_{-23.2\%}$	NNLO$_{\text{FTapprox}}$ QCD [12,14,15]
ggF HH (2026)	$30.40^{+7.25\%}_{-21.12\%} \pm 2.47\%$	$33.62^{+7.26\%}_{-21.04\%} \pm 2.43\%$	NNLO$_{\text{FTapprox}}$ with multiplicative N^{3}LO + N^{3}LL QCD corrections in the heavy-top limit and NLO EW corrections [21]
VBF HH	$1.684^{+0.05\%}_{-0.04\%} \pm 2.7\%$	$1.870^{+0.05\%}_{-0.03\%} \pm 2.7\%$	N^{3}LO QCD plus EW normalization [18–20]
ZHH	$0.365^{+3.3\%}_{-2.6\%} \pm 2.0\%$	$0.396^{+3.4\%}_{-2.7\%} \pm 1.9\%$	NNLO QCD [20,22]
W^+HH	$0.333^{+0.34\%}_{-0.41\%} \pm 2.3\%$	$0.357^{+0.36\%}_{-0.40\%} \pm 2.3\%$	NNLO QCD [20,22]
W^-HH	$0.172^{+1.3\%}_{-1.3\%} \pm 2.5\%$	$0.187^{+1.3\%}_{-1.4\%} \pm 2.5\%$	NNLO QCD [20,22]
$t\bar{t}HH$	$0.756^{+4.3\%}_{-15\%} \pm 3.4\%$	$0.860^{+4.2\%}_{-14\%} \pm 3.3\%$	NLO QCD [12,23]

Although subleading in rate, the other production modes summarized in Table 1 are sensitive to κ_λ through different interference structures and also provide access to additional interactions. VBF production provides the strongest direct sensitivity to the quartic interaction of two Higgs and two electroweak vector bosons, parameterized as $\kappa_{2V} \equiv g_{HHVV}/g^{\text{SM}}_{HHVV}$. The VHH process is also directly sensitive to $HHVV$ and can probe the $HHWW$ and $HHZZ$ interactions separately. The dependence of $t\bar{t}HH$ on κ_λ is weaker than in ggF and VBF, but this mode directly probes an anomalous $t\bar{t}HH$ contact interaction.

For the dominant gluon-fusion process, three developments since the 2019 review [5] are particularly relevant for the interpretation of Run 3 and HL-LHC measurements. First, the fixed-order frontier has moved: fully differential N^{3}LO predictions in the heavy-top limit, supplemented by the exact NLO top-quark-mass dependence, are now available [24], and NNLO+PS event generation with m_t corrections has been achieved in GENEVA [25], closing much of the gap between the best fixed-order predictions and the MC samples experiments actually fit. The main advance is a substantial reduction of the perturbative uncertainty. In the heavy-top limit, the new differential N^{3}LO calculation reduces the NNLO scale uncertainty by approximately a factor of three, bringing the residual perturbative uncertainty to the percent level before finite-top-mass effects are folded in [24].

Second, the complete NLO electroweak corrections are now available, including the top-Yukawa and self-coupling contributions [26], the light-quark two-loop pieces [27], and analytic results in the high-energy regime relevant for boosted topologies [28, 29]. Their kinematic dependence is especially important in the low-m_{HH}

region that drives the sensitivity to κ_λ: while the inclusive correction amounts to about -4%, it exceeds $+15\%$ near threshold and reaches about -10% at high m_{HH} [30].

Third, the dominant residual signal-theory uncertainty is now associated with the top-quark mass renormalization scheme. It is sizable and strongly asymmetric for the inclusive SM cross section, and can reach tens of percent at large m_{HH} or transverse momentum [15,21,31]. Predictions with alternative top-quark mass renormalization schemes are available at NLO matched to parton showers in the POWHEG framework [31], while NNLO calculations retaining the full top-quark-mass dependence are needed for a systematic assessment beyond NLO [15,32].

The N^{3}LO QCD and complete NLO electroweak corrections described above are not included in the reference normalization reported in Table 1, and used in the ATLAS and CMS analyses presented in this review. The updated 2026 LHCHWG recommendation [21] incorporates N^{3}LO+N^{3}LL QCD corrections in the heavy-top limit and NLO electroweak corrections multiplicatively, using PDF4LHC21. The corresponding cross-section predictions are listed separately in Table 1. It retains the NNLO$_{\mathrm{FTapprox}}$ scale uncertainty, while the uncertainty associated with the top-quark mass renormalization scheme remains the dominant contribution to the asymmetric uncertainty on the updated ggF prediction.

3. The Run 2 Legacy: Three Golden Channels

Anomalous values of the self-coupling can give similar inclusive rates while producing different m_{HH} spectra. The relative sensitivity of the experimental channels therefore depends not only on signal yield and background contributions, but also on their acceptance across m_{HH} and on how effectively their analysis strategies exploit this differential information, particularly at low m_{HH}.

The experimental searches are organized by the decay modes of the two Higgs bosons. Figure 2 shows the resulting matrix of final states and the broad program already covered by ATLAS and CMS. Branching fraction alone does not determine sensitivity: the available signal yield also depends on trigger acceptance, mass resolution, background composition, and the possibility of modeling that background from data.

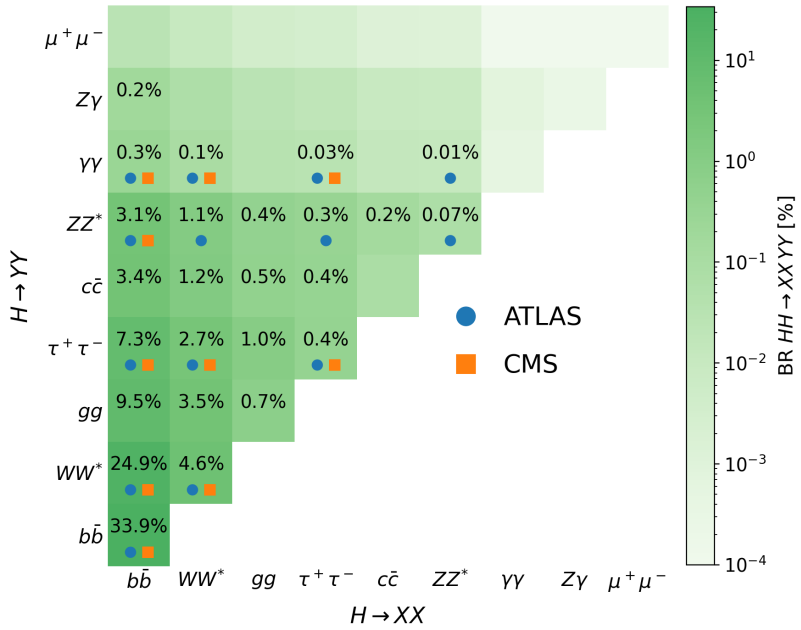


Figure 2. Branching ratios (BR) of the HH system into the leading final states, computed from the single-Higgs branching ratios. Each axis lists Higgs-boson decay modes in order of decreasing single-Higgs BR and each cell represents a combination of the two decays. The markers indicate the decay modes targeted in public non-resonant HH searches by ATLAS (blue circles) and CMS (orange squares); the numerical values are shown for all searched channels and for all BR $> 0.1\%$. The ATLAS-only markers for $WWZZ$, $ZZ\tau\tau$, $4Z$, and $\gamma\gamma ZZ$ correspond to channels included in the combined analysis of final states with leptons, τ leptons, and photons [33].

Figure 3 and Table 2 summarize the Run 2 results in the three channels that provide the strongest individual sensitivity by a substantial margin, dominate the combinations, and offer complementary sensitivity to κ_λ: $b\bar{b}b\bar{b}$, with the largest branching fraction but the overwhelming multijet background; $b\bar{b}\gamma\gamma$, with a very small branching fraction but excellent mass resolution and strong background rejection; and $b\bar{b}\tau^+\tau^-$, which lies between them in both signal rate and background complexity. They are the only final states for which both experiments obtain

expected upper limits below ten times the SM prediction. Their complementary reach in κ_λ is clearly visible in the two panels of Figure 3, showing that the best inclusive limit does not automatically provide the strongest constraint on the self-coupling. In both the ATLAS and CMS combinations, $b\bar{b}\gamma\gamma$ gives the narrowest expected single-channel interval on κ_λ, although it does not give the strongest expected limit on μ_{HH}. The Run 2 searches summarized in Table 2 provide interpretations of both ggF and VBF production, either through joint signal models or through dedicated categories and analyses. Their sensitivity to the SM HH rate is dominated by ggF, while dedicated VBF categories and boosted analyses provide sensitivity to κ_{2V}.

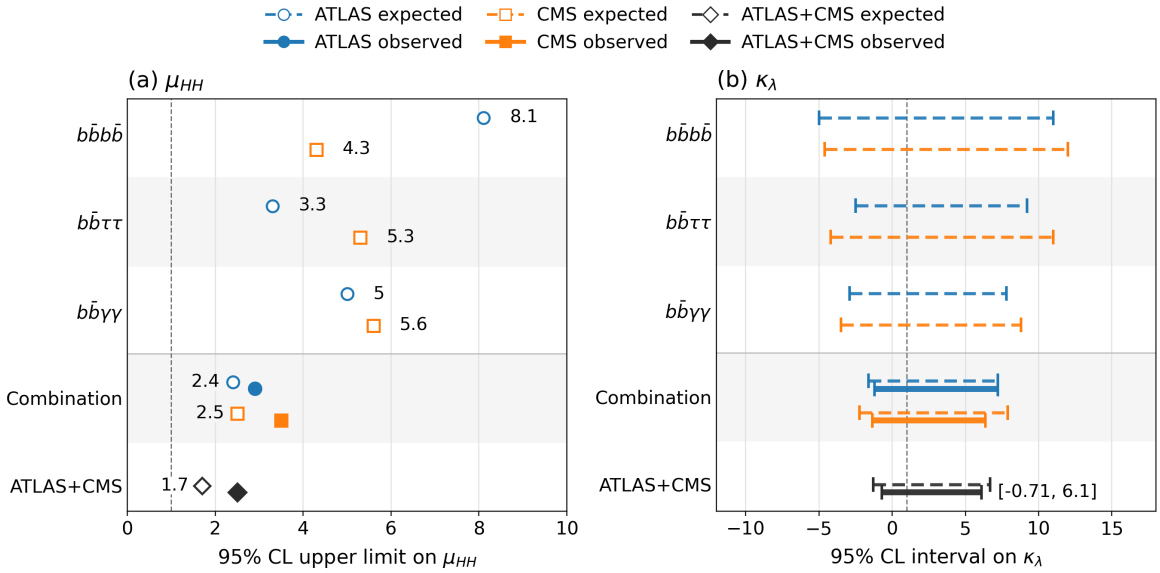


Figure 3. Summary of the 95% CL sensitivity to non-resonant HH production. (**a**) shows upper limits on the inclusive signal strength $\mu_{HH} = \sigma_{HH}/\sigma_{HH}^{\mathrm{SM}}$; (**b**) shows one-dimensional intervals on κ_λ with the other Higgs-coupling modifiers fixed to their SM values. Expected results are shown for the individual channels and combinations, while observed results are shown only for the ATLAS, CMS, and ATLAS+CMS combinations. The expected limits in (**a**) use the background-only hypothesis, while the expected intervals in (**b**) assume the SM HH signal. Open markers and dashed intervals denote expected results, while filled markers and solid intervals denote observed results. The combinations include additional final states beyond the three channels shown individually. The individual-channel points are the inputs as evaluated in the ATLAS, CMS, and joint combinations and can differ from the standalone results in Table 2 when analyses of the same final state are combined or updated [8,34,35]. For example, the CMS $b\bar{b}b\bar{b}$ point combines the resolved and boosted analyses.

Table 2. Summary of Run 2 legacy non-resonant HH results. Observed (expected) 95% CL upper limits on the signal strength $\mu_{HH} = \sigma_{HH}/\sigma_{HH}^{\mathrm{SM}}$, and observed constraints on κ_λ and κ_{2V} where reported.

Channel	Prod. Mode	Experiment	Lumi (fb^{-1})	Ref.	μ_{HH} obs (exp)	κ_λ (obs)	κ_{2V} (obs)
$b\bar{b}\gamma\gamma$	ggF + VBF	ATLAS	139	[36]	4.2 (5.7)	$[-1.5, 6.7]$	–
	ggF + VBF	ATLAS legacy	140	[37]	4.0 (5.0)	$[-1.4, 6.9]$	$[-0.5, 2.7]$
	ggF + VBF	CMS	137	[38]	7.7 (5.2)	$[-3.3, 8.5]$	$[-1.3, 3.5]$
$b\bar{b}\tau^+\tau^-$	ggF + VBF	ATLAS	139	[39]	4.7 (3.9)	–	–
	ggF + VBF	ATLAS legacy	140	[40]	5.9 (3.3)	$[-3.1, 9.0]$	$[-0.5, 2.7]$
	ggF + VBF	CMS	138	[41]	3.3 (5.2)	$[-1.7, 8.7]$	$[-0.4, 2.6]$
$b\bar{b}b\bar{b}$	ggF + VBF	ATLAS	126	[42]	5.4 (8.1)	$[-3.5, 11.3]$	$[0.0, 2.1]$
	ggF + VBF	CMS	138	[43]	3.9 (7.8)	$[-2.3, 9.4]$	$[-0.1, 2.2]$
	ggF	CMS legacy	138	[44]	10.0 (5.9)	$[-7.7, 16.2]$	–
	ggF + VBF	CMS boosted	138	[45]	9.9 (5.1)	$[-9.9, 16.9]$	$\kappa_{2V} = 0$ excl. 6.3σ
	VBF	ATLAS boosted	140	[46]	–	–	$[0.55, 1.49]$

The $b\bar{b}\gamma\gamma$ channel has the smallest branching fraction of the three, about 0.26%, but the diphoton trigger is more than 98% efficient after the offline selection [36], and the $m_{\gamma\gamma}$ resolution is 1–2%. The channel retains good acceptance at low m_{HH}, where the dependence on κ_λ is strongest, giving it greater sensitivity to the self-coupling than its inclusive-rate limit alone would suggest. The continuum background is determined from the diphoton-mass

sidebands, leaving resonant single-Higgs production, especially with heavy-flavor jets, as the principal irreducible background under the Higgs peak. ATLAS [36] and CMS [38] both use a modified four-object mass, defined using the reconstructed masses of the two Higgs-boson candidates, to divide the events into categories across the m_{HH} spectrum. CMS extracts the signal through a two-dimensional fit to $m_{\gamma\gamma}$ and m_{bb}, while ATLAS fits $m_{\gamma\gamma}$ separately in each category. The Run 2 results remain statistically limited, with the leading systematic contributions arising from the modeling of resonant single-Higgs production and the continuum background. Using the same full Run 2 dataset, ATLAS subsequently re-analysed the channel with event categories optimized for anomalous ggF and VBF kinematics, superseding the earlier non-resonant result [37]. The revised classification improves the expected 95% CL upper limit on μ_{HH} by 12% and reduces the widths of the expected intervals on κ_λ and κ_{2V} by 6% and 17%, respectively.

In the $b\bar{b}\tau^+\tau^-$ channel, neutrinos from the τ decays complicate the reconstruction of the $\tau\tau$ Higgs-boson candidate and of m_{HH}, while hadronic-τ trigger requirements reduce the acceptance at low m_{HH}, particularly below 400 GeV. The main backgrounds arise from $t\bar{t}$, Z+heavy-flavor production, and jets misidentified as hadronically decaying τ leptons. Both experiments use likelihood-based reconstructions of $m_{\tau\tau}$, based on the Missing Mass Calculator in ATLAS and SVfit in CMS, within multivariate signal extractions [39,41,47,48]. The Run 2 analyses remain statistically limited, with relevant systematic effects from background modeling and the calibration of τ identification and trigger efficiencies.

Using the same full Run 2 dataset, ATLAS subsequently re-analysed the channel with optimized low- and high-m_{HH} ggF categories, a dedicated VBF category, improved multivariate discriminants, and updated $t\bar{t}$ and Z+heavy-flavor background modeling. Based on a consistent statistical comparison with the previous analysis, ATLAS reports an improvement of about 15% in the expected 95% CL limit on μ_{HH} and reductions of 11% and 19% in the widths of the expected 95% confidence intervals on κ_λ and κ_{2V}, respectively [40].

The $b\bar{b}b\bar{b}$ channel contains about 34% of HH decays, but its signal is overwhelmed by a QCD multijet background several orders of magnitude larger. In the resolved topology, combinatorial choices in pairing the four b-jets broaden the reconstructed Higgs-boson mass peaks, while high p_{T} thresholds for the multijet triggers reduce the acceptance at low m_{HH}. The multijet background cannot be reliably modeled with simulation and is therefore modeled directly from data: the Run 2 ATLAS analysis reweights a two-tag control sample with a neural network [42], whereas CMS transfers a three-tag control sample to the four-tag signal region using BDT-based reweighting [43]. The finite size of the control samples and residual non-closure of these transfer methods are among the leading systematic uncertainties.

Boosted selections extend the sensitivity into the high-m_{HH} region, where resolved reconstruction loses efficiency, by identifying each $H \to b\bar{b}$ decay inside a large-radius jet. This topology is particularly sensitive to VBF production with anomalous κ_{2V}, which can be strongly enhanced at high m_{HH}. The CMS search includes both ggF and VBF production and excludes $\kappa_{2V} = 0$ at 6.3 standard deviations [45], while the ATLAS VBF-only analysis constrains $0.55 < \kappa_{2V} < 1.49$ and excludes $\kappa_{2V} = 0$ at 3.8 standard deviations [46]. The reconstruction and calibration developments that enabled these searches are discussed in Section 4.

The three golden channels achieve comparable Run 2 sensitivity through different experimental strategies. They remain statistically limited overall, but their leading systematic uncertainties are channel specific: the modeling of resonant single-Higgs and continuum backgrounds in $b\bar{b}\gamma\gamma$, top-quark and misidentified-τ backgrounds in $b\bar{b}\tau^+\tau^-$, and the data-derived multijet model in $b\bar{b}b\bar{b}$. The impact of these uncertainties on the first Run 3 results is discussed in Section 5.

Beyond the three golden channels, Figure 2 shows the broader LHC di-Higgs program. The ATLAS analysis targets the $b\bar{b}ZZ$, $4V$, $VV\tau\tau$, 4τ, $\gamma\gamma VV$, and $\gamma\gamma\tau\tau$ decay modes through signatures defined by their lepton, τ-lepton, and photon content. Their combination reaches an expected 95% CL upper limit of $\mu_{HH} < 11$, while considered separately, the non-photon and photon-enriched subsets reach $\mu_{HH} < 14$ and < 21, respectively [33]. The CMS multilepton analysis similarly combines contributions from the $4W$, $WW\tau\tau$, and 4τ decay modes and reaches $\mu_{HH} < 19.4$ [49]. Dedicated $b\bar{b}WW$ searches provide comparable sensitivity: CMS obtains an expected limit of $\mu_{HH} < 18$ [50], while the earlier ATLAS search in the $b\bar{b}\ell\nu\ell\nu$ signature, which also accepts contributions from $H \to ZZ^*$ and $H \to \tau\tau$, reaches $\mu_{HH} < 29$ [51]. The LHC sensitivity at 10–15 times the SM rate is therefore obtained by combining signatures that collect contributions from several low-branching-fraction decay modes, rather than from a single fourth dominant channel.

4. Machine Learning in Action: A Luminosity Multiplier

Machine learning first enters through the reconstructed objects, both online and offline, determining which events are recorded and selected and how precisely their kinematics are measured. Ref. [52] reviews the development of machine learning from detector reconstruction to real-time selection and final inference across LHC analyses.

In HH searches these stages are unusually closely connected: improved object reconstruction increases both the selected yield and the information available to the event classifier. All three golden channels contain at least one $H \to b\bar{b}$ decay. Their sensitivity therefore depends on identifying two b-jets, or four in $b\bar{b}b\bar{b}$, and reconstructing their energies. At a 70% per-jet efficiency, requiring four tags retains only 24% of the signal, so even modest improvements compound at event level. This section considers resolved and boosted object reconstruction and online selection: examples of machine learning for categorization, signal extraction, and background modeling are discussed with the results in Section 5.

4.1. Resolved Flavor Tagging

The Run 2 baselines were DL1r in ATLAS [53] and DeepJet in CMS [54], typically operated at b-jet efficiencies near 70% with light-jet misidentification probabilities around 1%. ATLAS progressed from DL1d to the transformer-based GN2 tagger, improving the measured c-jet and light-jet rejection by factors of approximately 3.5 and 1.8, respectively, at 70% b-jet efficiency [55]. In the CMS Run 3 $b\bar{b}b\bar{b}$ analysis, ParticleNet replaces the DeepJet tagger used in Run 2 and increases the absolute b-tagging efficiency by 3–7 percentage points at fixed misidentification probability [44]. ParticleNet uses graph convolutions over jet constituents, whereas its transformer-based successor UParT uses attention and pairwise interaction features [56–58]. UParT combines jet-flavor and hadronic-τ identification with flavor-aware jet-energy and resolution regression. In ATLAS, GN3 extends GN2 with neutral particle-flow objects and soft-lepton information; in simulation, it improves the c-jet and light-jet rejection by factors of approximately 1.8 and 2.4 relative to GN2 at 70% b-jet efficiency [59]. UParT v2 similarly improves the background rejection relative to its first release, by up to approximately a factor of two in the reported comparisons [58]. The ATLAS Carpe Datum study separately quantifies the gains available from substantially larger models and training-sample size: an 86-million-parameter tagger trained on 7.7 billion simulated jets improves the background rejection by approximately 40–50% at 77% b-jet efficiency relative to a 12-million-parameter model trained on 417 million jets, depending on the background flavor [60]. In the 308 fb^{-1} $b\bar{b}\gamma\gamma$ analysis, the use of GN2 improves the expected SM HH significance by approximately 20% [55,61]. The efficiencies and mistag probabilities are measured in data and propagated through scale factors and their uncertainties. These uncertainties are already controlled well enough that they do not dominate: in the CMS Run 3 $b\bar{b}b\bar{b}$ uncertainty decomposition, b-tagging uncertainties contribute 6% of the total uncertainty on μ_{HH} [44].

4.2. b-Jet Energy Reconstruction

The reconstructed m_{bb} resolution is degraded by neutrinos from semileptonic heavy-flavor decays and by radiation outside the jet clustering radius. CMS first introduced a dedicated b-jet energy regression in the Run 1 $VH(H \to b\bar{b})$ search [62,63], improving the dijet-mass resolution by about 15%, and now uses constituent-level regression within ParticleNet; in the recent $b\bar{b}b\bar{b}$ analysis the jet-p_{T} resolution improves by 10–25% and the reconstructed $H \to b\bar{b}$ mass resolution by about 20% [44]. ATLAS Run 2 analyses apply corrections for muons inside jets and a residual correction for out-of-cone energy losses for semileptonic b-hadron decays [36,64], while a recently developed transformer-based calibration improves the small-R b-jet resolution by 18–31% and the large-R jet momentum and mass resolution by 25–35% [65]. In the CMS Run 3 $b\bar{b}b\bar{b}$ fit, the combined jet-energy scale and resolution uncertainties contribute 5% of the total uncertainty on μ_{HH}. The underlying post-regression differences between data and simulation are 1–2% in the jet-energy scale and 4–8% in the resolution [44].

4.3. Boosted Reconstruction

At high m_{HH}, the two b quarks from a Higgs decay can merge into one large-radius jet. The constituent-level architectures used for resolved flavor tagging are especially important in this regime, where the tagger must identify both the two-prong substructure and its heavy-flavor content inside a single jet. In CMS, constituent-level taggers identify the two-prong heavy-flavor structure with signal efficiencies of about 40–50% and background rejection of $\mathcal{O}(10^2)$, while ATLAS uses a 60% efficiency working point with comparable rejection [45,46]. Their efficiencies and jet-mass response are calibrated in heavy-flavor-enriched and $Z(\to b\bar{b})$ samples; the remaining difficulty is the extrapolation to the highest transverse momenta, where the calibration data are sparse. Boosted reconstruction has already enabled the strongest direct constraints on κ_{2V} and will principally extend $b\bar{b}b\bar{b}$ and $b\bar{b}\tau^+\tau^-$ sensitivities. The same constituent-level strategy is being extended to merged hadronic $H \to \tau\tau$ decays, directly targeting boosted $b\bar{b}\tau^+\tau^-$ topologies [66,67]. Although the two studies use different signal definitions and event selections and therefore cannot be compared directly, the Run 2 boosted di-τ BDT retained about 60% of the signal at a multijet-rejection factor of 10^4, whereas the GN2X study reports 98% efficiency at a rejection factor of the same order [68].

4.4. Online Flavor Tagging and Trigger Acceptance

Hadronic HH decays compete with much larger multijet rates at the trigger. Real-time selections have become more inclusive under far harsher conditions, directly benefiting the low-m_{HH} region. The evolution is visible in the trigger menus. In ATLAS, the Run 3 $2b2j$ chain uses thresholds of 80, 55, 28, and 20 GeV with two online b tags, while the di-τ thresholds were lowered from 35/25 GeV in Run 2 to 30/20 GeV [69]. The real-time flavor tagging and asymmetric thresholds in the dedicated $2b2j$ chain increase the SM HH trigger efficiency by about 50% relative to the Run 2 trigger selections in $b\bar{b}b\bar{b}$ and $b\bar{b}\tau^+\tau^-$, with the largest recovery at low m_{HH} [69]. In CMS, the $b\bar{b}b\bar{b}$ thresholds evolved from 70/50/45/40 GeV with three online DeepCSV tags in Run 2 to 70/50/40/35 GeV with two ParticleNet tags in 2022. At fixed signal efficiency, the Run 3 tagger improves background rejection by about a factor of five and more than doubles the absolute $HH \to 4b$ trigger efficiency [44]. Data parking provides an additional gain: the 2023 parked stream accepts four jets above 30 GeV for delayed reconstruction [70], yielding an efficiency of about 82% for ggF $HH \to 4b$, among events with at least four offline jets above 30 GeV and $|\eta| < 2.5$, 60% higher than in Run 2 [70].

For hadronic-τ triggers, CMS used online DeepTau in 2022–2023 [71] and moved to ParticleNet in 2024, which provides higher efficiency at a comparable trigger rate and enables lower online thresholds [72]. A complementary di-τ+jet path lowers the τ_h threshold by 5 GeV, while data parking was extended to $b\bar{b}\tau^+\tau^-$ with a four-jet path requiring online τ and b tags [72, 73]. These gains enlarge the recorded signal phase space before any offline selection is applied. For comparison, the CMS Run 1 trigger required four jets above 30 GeV, including two above 80 GeV, and two online b tags at an average pileup of 21 [74], while the Run 3 parked stream reaches uniform 30 GeV thresholds despite the substantially higher pileup.

The combined effect of these developments is quantified by the same-data comparisons in Section 5. The remaining machine-learning applications act at event level: assigning jets to Higgs candidates, defining analysis categories, separating several signal and background processes, and transferring data-derived background models.

5. Run 3: Sensitivity beyond Luminosity Scaling

Building on the Run 2 analysis strategy established in Section 3, the first Run 3 and Run 2+3 results separate two sources of progress that are otherwise difficult to distinguish: a larger dataset and a more sophisticated analysis strategy. The cleanest tests are re-analyses of the same Run 2 collisions, for which any gain must come from reconstruction, classification, or background treatment. For a fixed analysis dominated by statistical uncertainties, the expected upper limit decreases approximately as $1/\sqrt{L}$, while additional systematic uncertainties would slow the scaling further. Figure 4 places this reference beside the luminosity accumulated at the LHC. In all three golden channels, the published limits improve faster than $1/\sqrt{L}$, showing the additional gain from improvements in reconstruction, triggering, event classification, and background modeling. For $b\bar{b}b\bar{b}$, this progression also reflects the inclusion of boosted categories, which are absent from the Run 2 reference point. An illustrative extrapolation of the progression in Figure 4 suggests that, if they are retained in the channel combinations, the complete Run 2 + 3 dataset could reach an expected limit close to the SM rate, before the full HL-LHC dataset is accumulated. Only a few years ago, this level of sensitivity was expected to require the HL-LHC program.

The $b\bar{b}b\bar{b}$ analysis provides the most complete example of machine learning acting at every stage. The CMS result based on 62 fb^{-1} at 13.6 TeV reaches observed and expected 95% CL upper limits of $\mu_{HH} < 4.4$; with less than half the Run 2 luminosity, its resolved analysis reduces the expected limit at equivalent luminosity by more than 50%, through the trigger-acceptance gains discussed in Section 4 together with improved event selection and signal extraction [44]. Reprocessing the 138 fb^{-1} Run 2 sample with the new method improves the expected limit on μ_{HH} by about 25% on identical data. Beyond the online and offline ParticleNet reconstruction discussed in Section 4, a transformer signal classifier uses the relations between jet pairs as inputs. Those pairwise inputs improve the analysis sensitivity by approximately 25%, while the classifier rejects the background by two orders of magnitude while retaining about 40% of the SM signal, and by three orders of magnitude while retaining about 10%. In an alternative resolved-analysis approach, a graph-based multiclassifier simultaneously separates ggF and VBF HH from ZZ, ZH, and multijet production, and a neural-network reweighting transports the data control sample into the signal region. Dedicated ZZ and ZH fits validate the background model and signal extraction using known SM processes [44]. The 13 and 13.6 TeV combination reaches an observed (expected) 95% CL upper limit of $\mu_{HH} < 4.7$ (2.8). For the Run 3 result, the statistical and systematic components contribute 79% and 61%, respectively, to the total post-fit uncertainty on μ_{HH}. The quoted impacts are correlated and are not independent contributions to the total uncertainty. The systematic component is dominated by the finite size of the control samples in data used to derive the background shape (41%), its normalization (30%), and statistical fluctuations in individual bins (23%) [44].

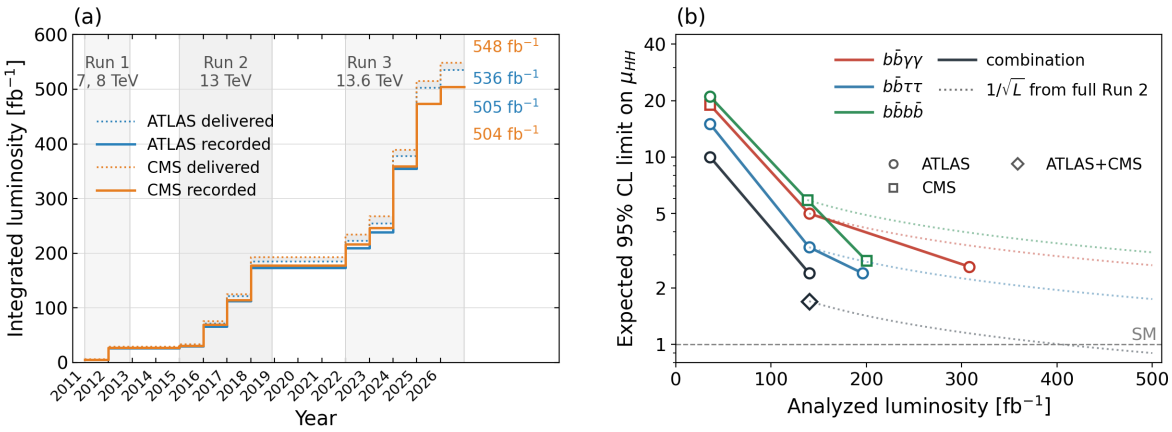


Figure 4. (**a**) Cumulative integrated luminosity delivered to and recorded by ATLAS and CMS as a function of year; the gray band spans the luminosities delivered to the two experiments. The record 125.4 fb^{-1} proton run of 2025 and the partial 2026 dataset are not yet represented in the analyses shown in (**b**) [9,10]. (**b**) Evolution of the expected 95% CL upper limit on the HH signal strength for each of the three golden channels and their combinations. Circles denote ATLAS, squares CMS, and the diamond the joint ATLAS + CMS combination. Only the most sensitive public result from either ATLAS or CMS is shown. The dotted curves show the $1/\sqrt{L}$ scaling expected for a statistically limited analysis, normalized to the full Run 2 result in each channel. Where a dataset has been reanalyzed, only the most recent result is shown [5,8,37,38,40,44,61,75]. The extrapolation is illustrative as the analyses shown differ in their level of development and optimization.

In $b\bar{b}\gamma\gamma$, ATLAS combines 140 fb^{-1} at 13 TeV and 168 fb^{-1} at 13.6 TeV [61]. ATLAS measures $\mu_{HH} = 0.9^{+1.4}_{-1.1} = 0.9^{+1.3}_{-1.0}\,(\text{stat.})^{+0.5}_{-0.5}\,(\text{syst.})$ and sets an observed (expected) 95% CL upper limit of $\mu_{HH} < 3.7$ (2.6). The same analysis constrains $-1.6 < \kappa_\lambda < 6.6$ ($-1.8 < \kappa_\lambda < 6.9$ expected) at 95% CL. A single channel now provides an expected κ_λ interval comparable to the five-channel ATLAS Run 2 combination of Section 3 ($-1.6 < \kappa_\lambda < 7.2$ expected) [34]. Relative to the Run 2 analysis, the expected significance improves by approximately 20% from GN2 flavor tagging and by a further 5% from the kinematic fit. The additional data provide an improvement in expected significance of approximately 60%, including 50% from the increased event sample and 10% from the re-optimized analysis categories [61]. The total uncertainty remains statistically dominated. The largest relative impacts on the signal strength arise from the QCD-scale, top-quark mass renormalization scheme, and PDF+α_s signal uncertainties (up to 35%), the heavy-flavor content of single-Higgs production (30%), the photon energy scale (up to 34%), and parton-shower modeling (15%) [61]. The CMS analysis of 61.9 fb^{-1} tests two ways of assigning mass information between the classifier and the likelihood [76]. The two-dimensional $(m_{\gamma\gamma}, m_{bb})$ fit has the stronger expected 95% CL upper limit, $\mu_{HH} < 7.3$, compared with $\mu_{HH} < 8.7$ for the one-dimensional fit. Heavy-flavor single-Higgs production modeling is an important uncertainty in both analyses. In CMS, the modeling of the continuum background is also a central systematic issue. The $b\bar{b}H$ contribution is assigned a 50% normalization uncertainty, and the fit-function bias assigned in the two-dimensional strategy ranges from 3% to 30% across categories [76].

In $b\bar{b}\tau^+\tau^-$, the Run 2 reoptimization improved the expected 95% CL upper limit on μ_{HH} by about 15% without additional data through a dedicated VBF category, revised control selections, and improved multivariate classification [40]. The subsequent analysis of 196 fb^{-1}, including 56 fb^{-1} at 13.6 TeV, reaches an expected 95% CL upper limit of $\mu_{HH} < 2.4$, the strongest expected sensitivity reported by a single channel [75]. The observed upper limit is $\mu_{HH} < 5.3$. The fitted signal strength is $\mu_{HH} = 2.6^{+1.4}_{-1.0} = 2.6^{+1.0}_{-0.9}\,(\text{stat.})^{+1.0}_{-0.5}\,(\text{syst.})$. The average total uncertainty is 1.20, with statistical and systematic components of 0.91 and 0.76, respectively, and the observed significance is 2.6σ.

In the most sensitive classifier bin, tW production constitutes about 24% of the background. At NLO, tW and $t\bar{t}$ production share doubly resonant contributions, so their separation in simulation requires a modeling prescription. The difference between the diagram-removal and diagram-subtraction prescriptions gives the largest individual uncertainty in the tW model. The leading systematic uncertainties are the ggF HH cross-section uncertainty from QCD-scale and top-quark mass renormalization scheme variations, heavy-flavor modeling in ggH production, the tW–$t\bar{t}$ interference, and the statistical precision of the background templates in the most signal-like bins. The uncertainties in HH, other single-Higgs and tW modeling, and in the background-template statistics, contribute 0.54, 0.25, 0.21, and 0.21, respectively, to the total uncertainty of 1.20 on μ_{HH}. Including systematic uncertainties

weakens the expected upper limit on μ_{HH} by 21% [75]. The measurements of ZH and ZZ in the same final state, and with the same event selection, provide direct validation of the event reconstruction and background separation. In particular, the ZH measurement establishes the first evidence for this process in the $b\bar{b}\tau^+\tau^-$ final state, with an observed significance of 3.5σ [75]. The observed 95% CL κ_λ interval splits into two components, $[-3.4, 1.6] \cup [5.5, 10.1]$, compared with an expected interval of $[-1.7, 8.5]$. The disconnected observed interval reflects the non-monotonic dependence of the ggF rate and the m_{HH} spectrum on κ_λ, for which separated values of κ_λ can give similar signal predictions. CMS has also released a preliminary Run 2 + 3 $b\bar{b}\tau^+\tau^-$ result using 310 fb^{-1}, setting an expected 95% CL upper limit of $\mu_{HH} < 3.0$ [73]. Relative to the Run 2 strategy described in Section 3, the ParticleNet-based di-τ_h trigger, the lower-threshold di-τ_h + jet path, a dedicated boosted-$\tau_h\tau_h$ channel and data parking increase the hadronic-τ acceptance. As in ATLAS, the result remains statistically dominated, with signal and single-Higgs modeling among the leading systematic effects. Note that CMS does not report a separate impact from tW–$t\bar{t}$ interference.

Continuing the pattern seen in Run 2, the preliminary results including Run 3 data show that while $b\bar{b}\tau^+\tau^-$ gives the slightly stronger expected limit on μ_{HH}, $b\bar{b}\gamma\gamma$ provides the narrower expected constraints on κ_λ.

Beyond these leading channels, the machine learning-driven improvements, reviewed in Section 4, can produce large relative gains in channels that are not yet individually competitive. The CMS $b\bar{b}WW$ Run 3 search reaches an expected 95% CL upper limit of $\mu_{HH} < 18.5$ with 62 fb^{-1}, comparable to the expected $\mu_{HH} < 18$ from the full-Run 2 analysis [50, 77]. A staged multiclass and binary neural-network selection improves the sensitivity, evaluated through the expected upper limit on μ_{HH}, by approximately 50% at fixed dataset size, while the trigger increases the signal yield by up to 17% in the most sensitive bins. The HH program is also expanding beyond inclusive ggF and VBF production. Associated-production searches remain at an earlier stage. The current direct VHH limits still come from the full Run 2 datasets: ATLAS, with 139 fb^{-1}, sets an observed (expected) 95% CL upper limit of $\mu_{VHH} < 183$ (87), while CMS, with 138 fb^{-1}, obtains $\mu_{VHH} < 294$ (124) [78, 79]. By contrast, the first $t\bar{t}HH$ search, using 196 fb^{-1} of ATLAS Run 2 + 3 data, combines three final states and sets an observed (expected) 95% CL upper limit of $\mu_{t\bar{t}HH} < 20$ (21) [80]. The preliminary CMS search uses a smaller dataset, 138 fb^{-1} from Run 2, and covers only the single-lepton $HH \to 4b$ channel, setting a less stringent observed (expected) 95% CL upper limit of $\mu_{t\bar{t}HH} < 49$ (55) [81]. These sensitivities remain far from the SM rates, but they probe interactions not accessible through ggF alone: VHH probes the $HHWW$ and $HHZZ$ interactions separately, complementing the sensitivity of VBF to their common modifier, while $t\bar{t}HH$ directly constrains the $t\bar{t}HH$ contact interaction.

Across the current results, statistical uncertainty remains the largest, but systematic uncertainties already have a sizable, channel-dependent impact: the leading effects arise from the data-driven multijet prediction in $b\bar{b}b\bar{b}$, top-background and signal modeling in $b\bar{b}\tau^+\tau^-$, and signal theory and heavy-flavor single-Higgs modeling in $b\bar{b}\gamma\gamma$. The measurements are therefore not yet systematically limited, but further gains will depend on whether these channel-specific uncertainties decrease as the data sample grows.

6. Beyond κ_λ: Effective Field Theory

The one-dimensional self-coupling limits quoted above fix all other Higgs interactions to their SM values. Even if the only departures from the SM are rescalings of the top Yukawa coupling, $\kappa_t \equiv y_t/y_t^{\text{SM}}$, and the trilinear Higgs coupling, the ggF amplitude depends on both: $\mathcal{A} = \kappa_t^2\mathcal{A}_1 + \kappa_t\kappa_\lambda\mathcal{A}_2$. The corresponding cross section is

$$\sigma_{pp\to HH}(\kappa_t, \kappa_\lambda) \propto \kappa_t^4 \left[\overline{|\mathcal{A}_1|^2} + 2\,\frac{\kappa_\lambda}{\kappa_t}\,\Re\overline{\mathcal{A}_1\mathcal{A}_2^*} + \left(\frac{\kappa_\lambda}{\kappa_t}\right)^2 \overline{|\mathcal{A}_2|^2} \right], \tag{2}$$

where the bars denote phase-space averages [5]. The m_{HH} shape primarily constrains the ratio κ_λ/κ_t, while the absolute rate provides the overall κ_t^4 dependence. One-dimensional κ_λ intervals quoted by the experiments rely on fixing κ_t to its SM value. Relaxing this assumption introduces correlations and ambiguities that can only be reduced with additional information, including single-Higgs measurements. Effective field theory (EFT) provides a systematic extension beyond the simple self-coupling-modifier scans by organizing the effects of unresolved new physics in higher-dimensional operators. In the Standard Model EFT (SMEFT), the Higgs remains part of an $SU(2)_L$ doublet and

$$\mathcal{L}_{\text{SMEFT}} = \mathcal{L}_{\text{SM}} + \sum_i \frac{C_i^{(6)}}{\Lambda^2}\mathcal{O}_i^{(6)} + \mathcal{O}(\Lambda^{-4}). \tag{3}$$

For gluon-fusion HH production, the leading dimension-six dependence can be written schematically as:

$$\mathcal{A}_{\mathrm{SMEFT}}(gg \to HH) = \mathcal{A}_{\mathrm{SM}} + \frac{C_H}{\Lambda^2}\mathcal{A}_H + \frac{C_{tH}}{\Lambda^2}\mathcal{A}_{tH} + \frac{C_{HG}}{\Lambda^2}\mathcal{A}_{HG} + \frac{C_{tG}}{\Lambda^2}\mathcal{A}_{tG} + \mathcal{O}(\Lambda^{-4}). \quad (4)$$

Here C_H modifies the Higgs potential, C_{tH} correlates the $t\bar{t}H$ and $t\bar{t}HH$ interactions, C_{HG} correlates the effective ggH and $ggHH$ vertices, and C_{tG} is the top-quark chromomagnetic interaction. The correlations are a predictive feature of SMEFT: the same coefficients can be constrained by HH, single-Higgs, top, and electroweak measurements. However, these correlations also make the interpretation dependent on the operator basis, the scale, and whether terms quadratic in the dimension-six coefficients are retained. The Higgs EFT (HEFT) makes fewer assumptions about electroweak symmetry breaking. Electroweak symmetry is realized non-linearly, with the physical Higgs field treated as a singlet, allowing the HHH, $t\bar{t}H$, $t\bar{t}HH$, ggH, and $ggHH$ interactions to vary independently. The leading gluon-fusion amplitude is then:

$$\mathcal{A}(gg \to HH) = c_{tth}^2\mathcal{A}_{\square} + c_{tth}c_{hhh}\mathcal{A}_{\triangle} + c_{tthh}\mathcal{A}_{t\bar{t}HH} + c_{ggh}c_{hhh}\mathcal{A}_{ggh} + c_{gghh}\mathcal{A}_{gghh}. \quad (5)$$

The HEFT cross section obtained from Equation (5) contains terms up to fourth order in these five coefficients and includes interference among the amplitude structures. Unlike SMEFT, it does not impose the correlations between single- and double-Higgs vertices. The m_{HH} spectrum remains a key observable, as different coefficient combinations can have similar inclusive rates but distinguishable effects on the mass spectrum. The theory predictions needed for these interpretations have advanced substantially. Full NLO QCD SMEFT predictions for $gg \to HH$ now include a systematic treatment of truncation ambiguities [82], with extensions to the chromomagnetic and four-top operators [83], renormalization-group evolution between matching and measurement scales [84], and the γ_5-scheme dependence of sub-leading operators [85]. These calculations also make it possible to test quantitatively whether a linear SMEFT expansion at the order retained is adequate for the deformations accessible in HH, or whether a non-linear HEFT description provides a more appropriate description [86].

Experimentally, the ATLAS $b\bar{b}\gamma\gamma$ program is one of the most developed examples. Its Run 2 analysis constrains κ_λ and κ_{2V} together with SMEFT and HEFT coefficients [37]. The 308 fb^{-1} interpretation extends the SMEFT treatment to operators affecting ggF and VBF production, propagates their effects to the $H \to \gamma\gamma$ and $H \to b\bar{b}$ branching fractions, and profiles HEFT coefficients in one- and two-dimensional scans [87]. The CMS combination likewise reports HEFT benchmark scans and constraints on ultraviolet-complete models [35]. These results are a first step from one-parameter limits toward fits of correlated coupling structures; they do not yet determine the full coefficient set simultaneously. Single-Higgs measurements constrain κ_λ through electroweak loop corrections and are therefore complementary to direct HH production. Their standalone sensitivity is not yet competitive with the direct searches, and the result is model dependent because other coupling and EFT effects enter the same observables. Their principal value here is to constrain κ_t and other correlated coefficients that are degenerate in HH alone [88,89]. The CMS $b\bar{b}\gamma\gamma$ analysis illustrates the point by using $t\bar{t}H(\gamma\gamma)$-enriched categories to perform an in-situ $(\kappa_\lambda, \kappa_t)$ fit [38]. For $\kappa_\lambda = 1$, adding these categories reduces the expected 68% uncertainty on κ_t from $^{+0.4}_{-1.2}$ to ± 0.2 and substantially reduces the degeneracy in the two-dimensional likelihood.

As the coefficient phase space expands, single-Higgs-enriched regions are increasingly included as part of the same likelihood as the HH signal regions. This improves the global constraint on operators such as C_H [90], but also makes the self-coupling interpretation dependent on the theory modeling of ggF and $t\bar{t}H$ production and of the Higgs transverse-momentum spectrum. The interpretation will therefore require both the direct information from HH production and the broader, more model-dependent constraints from precision single-Higgs data.

7. Outlook

The approved HL-LHC program will deliver approximately $3\,\mathrm{ab}^{-1}$ of pp collisions at 14 TeV to each experiment [91]. The ATLAS and CMS projection for the 2026 European Strategy update gives a combined HH significance of about 7.6σ and $0.74 < \kappa_\lambda < 1.29$ at 68% CL, when the remaining couplings are fixed to their SM values [11,92].

In the terminology introduced in ref. [5], bronze, silver, gold, and platinum denote approximately $\mathcal{O}(100\%)$, 25–50%, 5–10%, and 1% precision on the self-coupling. Electroweak baryogenesis does not imply a model-independent target precision on κ_λ. In simple deformations of the potential, a strong first-order transition is associated with order-one shifts in κ_λ, while higher-order terms or additional scalar dynamics can substantially modify this relation [93]. A measurement with $\mathcal{O}(20\%)$ precision can test some electroweak-baryogenesis scenarios, whereas sensitivity approaching $\mathcal{O}(1\%)$ may be needed to probe more difficult first-order-transition scenarios [6]. Gold and platinum should therefore be understood as progressively broader tests of potential deformations, not as model-independent phase-transition thresholds.

The HL-LHC is therefore projected to reach the silver benchmark: observation of HH and a first quantitative direct test of the potential, including sensitivity to some of the order-one deformations associated with a strong first-order transition, but not yet sensitivity to deviations at the 5–10% scale associated with the gold benchmark. Figure 5 shows that the projection changed from about 4σ in 2020 to more than 7σ in 2026. For the updated projection, theory uncertainties are halved, contributions from finite simulated samples are neglected, and experimental uncertainties are scaled according to their origin [92]. The projections also assume 5% improvements in b-tagging and hadronic-τ identification efficiencies. The broader change from the 2020 to the 2026 projection includes improved analysis inputs, led by machine-learning-driven developments, including resolved and boosted categories [92]. The projection still depends on controlling the same limitations exposed by the current analyses: the top-quark mass renormalization scheme and signal shape at large m_{HH}, the transfer of the multijet background in $b\bar{b}b\bar{b}$, top and misidentified-τ backgrounds in $b\bar{b}\tau^+\tau^-$, and heavy-flavor single-Higgs production in $b\bar{b}\gamma\gamma$.

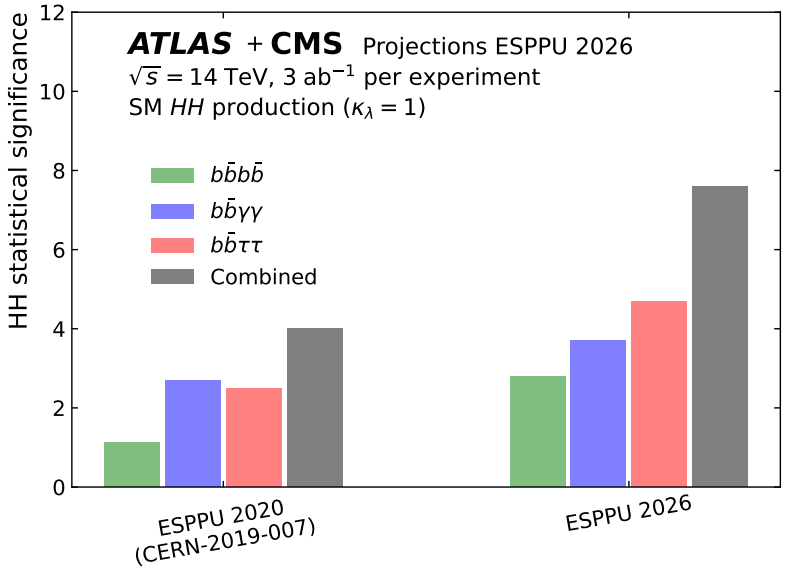


Figure 5. Comparison of the ESPPU 2020 and ESPPU 2026 projected ATLAS+CMS HH significances at $3\,\mathrm{ab}^{-1}$ per experiment [92]. The updated projection turns the HL-LHC expectation from evidence-level sensitivity into observation-level sensitivity, with the largest relative gain in $b\bar{b}b\bar{b}$.

No collider beyond the HL-LHC has yet been approved, but the proposals assessed for the 2026 European Strategy illustrate how the measurement could progress beyond silver sensitivity [11]. An e^+e^- Higgs factory below the HH threshold accesses κ_λ indirectly through loop corrections to several single-Higgs cross sections and decay rates. FCC-ee projections give approximately 28% precision in the baseline standalone fit and 18% when combined with the direct HL-LHC information; a doubled-luminosity scenario approaches 15% [94]. The extraction remains indirect and more model dependent than HH production, so its strongest use is in combination with the LHC rather than as a replacement for it.

Above the HH threshold, an e^+e^- collider adds two direct production mechanisms. A linear collider at 550 GeV is projected to reach approximately 11% precision with 8 ab^{-1} by combining ZHH and $\nu\bar{\nu}HH$ [95]. Updated reconstruction, transformer flavor tagging, and event selection account for a substantial part of this reach: at 500 GeV the projected ZHH cross-section precision improves from 21.1% to 16.6% [96]. More importantly, the two processes respond differently to κ_λ. Their constructive and destructive interference patterns provide sensitivity in regions where the $gg \to HH$ rate is locally flat and reduce the multiple solutions that can remain in the LHC likelihood. The resulting information is therefore complementary both experimentally and at the amplitude level, and approaches the gold benchmark. The complementarity is especially pronounced near $\kappa_\lambda \simeq 2$, where the LHC ggF rate loses sensitivity while the lepton-collider cross sections retain a steep dependence on κ_λ [96].

Higher collider energies would turn the self-coupling into a precision observable: FCC-hh at 100 TeV projects 3–4% precision and direct sensitivity to the quartic coupling through HHH, while a 10 TeV muon collider projects few-percent precision through vector-boson-fusion HH [11]. These projections enter the gold regime; the percent-level platinum benchmark remains beyond the programs considered here.

8. Conclusions

Higgs-boson pair production provides direct experimental access to the Higgs self-interaction and, through it, to the Higgs potential. Measuring both the pair-production rate and the invariant-mass distribution tests the strength of the trilinear Higgs coupling and its impact on the kinematics of the process, providing a direct probe of the SM Higgs potential. Since the 2019 review, HH searches have progressed from order-of-magnitude limits to the first joint measurement of μ_{HH}, with expected sensitivity approaching the SM rate. The first results including Run 3 data improve faster than expected from luminosity alone, showing the effect of improved machine learning-driven object reconstruction, triggers, event classification, and background modeling. An illustrative extrapolation suggests that the Run 2 + 3 dataset could approach sensitivity to the SM rate before the full HL-LHC dataset is accumulated. At the HL-LHC, the combined analyses are expected to observe HH production and constrain κ_λ at approximately the 25–30% level around the SM value. This will test large modifications of the Higgs potential. Future colliders would add production mechanisms with different dependence on the self-coupling. This complementarity can move the program beyond the silver benchmark toward gold, extending sensitivity to smaller potential deformations for which the connection to the electroweak phase transition becomes increasingly model dependent. Di-Higgs production measurements will test a defining property of the only known elementary scalar particle: whether the Higgs field interacts with itself as required by the mechanism that breaks electroweak symmetry, or whether its potential carries evidence of additional dynamics.

Funding

Caterina Vernieri is supported by the U.S. Department of Energy under Contract No. DE-AC02-76SF00515.

Conflicts of Interest

The author declares no conflict of interest.

Use of AI and AI-Assisted Technologies

During the preparation of this review, the author used Codex (OpenAI) to assist with text editing and plot formatting. The author reviewed and edited the material and takes full responsibility for the content of the published article.

References

1. ATLAS Collaboration. Observation of a new particle in the search for the Standard Model Higgs boson with the ATLAS detector at the LHC. *Phys. Lett. B* **2012**, *716*, 1. https://doi.org/10.1016/j.physletb.2012.08.020.
2. CMS Collaboration. Observation of a new boson at a mass of 125 GeV with the CMS experiment at the LHC. *Phys. Lett. B* **2012**, *716*, 30. https://doi.org/10.1016/j.physletb.2012.08.021.
3. ATLAS Collaboration. Combined measurement of the Higgs boson mass from the $H \to \gamma\gamma$ and $H \to ZZ^* \to 4\ell$ decay channels with the ATLAS detector using $\sqrt{s} = 7$, 8 and 13 TeV pp collision data. *Phys. Rev. Lett.* **2023**, *131*, 251802. https://doi.org/10.1103/PhysRevLett.131.251802.
4. Hayrapetyan, A.; Tumasyan, A.; Adam, W.; et al. Measurement of the Higgs boson mass and width using the four-lepton final state in proton-proton collisions at $\sqrt{s} = 13$ TeV. *Phys. Rev. D* **2025**, *111*, 092014. https://doi.org/10.1103/PhysRevD.111.092014.
5. Di Micco, B.; Gouzevitch, M.; Mazzitelli, J.; et al. Higgs boson potential at colliders: status and perspectives. *Rev. Phys.* **2020**, *5*, 100045. https://doi.org/10.1016/j.revip.2020.100045.
6. Dawson, S.; Meade, P.; Ojalvo, I.; et al. Report of the Topical Group on Higgs Physics for Snowmass 2021: The Case for Precision Higgs Physics. *arXiv* **2022**, arXiv:2209.07510.
7. Narain, M.; Reina, L.; Tricoli, A.; et al. The Future of US Particle Physics: The Snowmass 2021 Energy Frontier Report. *arXiv* **2022**, arXiv:2211.11084.
8. ATLAS Collaboration; CMS Collaboration. Combination of ATLAS and CMS searches for Higgs boson pair production at $\sqrt{s} = 13$ TeV. *Phys. Rev. Lett.* **2026**, *137*, 131803. https://doi.org/10.1103/27s7-2frt.
9. ATLAS Collaboration. Public ATLAS Online Luminosity Plots for Run-3 of the LHC. ATLAS Public Results. 2026. Available online: https://twiki.cern.ch/twiki/bin/view/AtlasPublic/LuminosityPublicResultsRun3 (accessed on 15 July 2026).
10. CMS Collaboration. Public CMS Luminosity Information. CMS Public Results. 2026. Available online: https://twiki.cern.ch/twiki/bin/view/CMSPublic/LumiPublicResults (accessed on 15 July 2026).
11. de Blas, J.; Dunford, M.; Bagnaschi, E.; et al. (Eds.) Physics Briefing Book: input for the 2026 update of the European Strategy for Particle Physics. In *CERN Yellow Reports: Monographs*; CERN: Geneva, Switzerland, 2025; Volume 8. https://doi.org/10.23731/CYRM-2025-008.
12. LHC Higgs Working Group. *Current Recommendations for HH Cross-Sections*; LHC Higgs WG4 Technical Report; CERN: Geneva, Switzerland, 2026.

13. Borowka, S.; Greiner, N.; Heinrich, G.; et al. Higgs boson pair production in gluon fusion at next-to-leading order with full top-quark mass dependence. *Phys. Rev. Lett.* **2016**, *117*, 012001. https://doi.org/10.1103/PhysRevLett.117.012001. Erratum in *Phys. Rev. Lett.* **2016**, *117*, 079901.
14. Grazzini, M.; Heinrich, G.; Jones, S.; et al. Higgs boson pair production at NNLO with top quark mass effects. *J. High Energy Phys.* **2018**, *5*, 059. https://doi.org/10.1007/JHEP05(2018)059.
15. Baglio, J.; Campanario, F.; Glaus, S.; et al. $gg \to HH$: combined uncertainties. *Phys. Rev. D* **2021**, *103*, 056002. https://doi.org/10.1103/PhysRevD.103.056002.
16. Heinrich, G.; Jones, S.P.; Kerner, M.; et al. NLO predictions for Higgs boson pair production with full top quark mass dependence matched to parton showers. *J. High Energy Phys.* **2017**, *8*, 088. https://doi.org/10.1007/JHEP08(2017)088.
17. Heinrich, G.; Jones, S.P.; Kerner, M.; et al. Probing the trilinear Higgs boson coupling in di-Higgs production at NLO QCD including parton shower effects. *J. High Energy Phys.* **2019**, *6*, 066. https://doi.org/10.1007/JHEP06(2019)066.
18. Dreyer, F.A.; Karlberg, A. Vector-boson fusion Higgs pair production at N^3LO. *Phys. Rev. D* **2018**, *98*, 114016. https://doi.org/10.1103/PhysRevD.98.114016.
19. Dreyer, F.A.; Karlberg, A.; Lang, J.N.; et al. Precise predictions for double-Higgs production via vector-boson fusion. *Eur. Phys. J. C* **2020**, *80*, 1037. https://doi.org/10.1140/epjc/s10052-020-08610-7.
20. Gröber, R.; Karlberg, A.; Pellen, M.; et al. Electroweak Higgs boson pair production: Updated inclusive cross sections. *SciPost Phys. Commun. Rep.* **2026**, *27*. https://doi.org/10.21468/SciPostPhysCommRep.27.
21. Ajjath, A.H.; Alioli, S.; Bagnaschi, E.; et al. Higgs Boson Pair Production via Gluon Fusion: Higher-Order Corrections and Theoretical Uncertainties. *arXiv* **2026**, arXiv:2609.04868.
22. Baglio, J.; Djouadi, A.; Gröber, R.; et al. The measurement of the Higgs self-coupling at the LHC: Theoretical status. *J. High Energy Phys.* **2013**, *4*, 151. https://doi.org/10.1007/JHEP04(2013)151.
23. Frederix, R.; Frixione, S.; Hirschi, V.; et al. Higgs pair production at the LHC with NLO and parton-shower effects. *Phys. Lett. B* **2014**, *732*, 142. https://doi.org/10.1016/j.physletb.2014.03.026.
24. Chen, X.; Dai, Y.; Li, H.T.; et al. Fully differential Higgs boson pair production at N^3LO with top quark mass effects. *J. High Energy Phys.* **2026**, *6*, 005. https://doi.org/10.1007/JHEP06(2026)005.
25. Alioli, S.; Marinelli, G.; Napoletano, D. NNLO+PS double Higgs boson production with top-quark mass corrections in GENEVA. *J. High Energy Phys.* **2025**, *9*, 206. https://doi.org/10.1007/JHEP09(2025)206.
26. Heinrich, G.; Jones, S.; Kerner, M.; et al. Electroweak corrections to Higgs boson pair production: the top-Yukawa and self-coupling contributions. *J. High Energy Phys.* **2024**, *11*, 040. https://doi.org/10.1007/JHEP11(2024)040.
27. Bonetti, M.; Rendler, P.; Torres Bobadilla, W.J. Two-loop light-quark electroweak corrections to Higgs boson pair production in gluon fusion. *J. High Energy Phys.* **2025**, *7*, 024. https://doi.org/10.1007/JHEP07(2025)024.
28. Davies, J.; Schönwald, K.; Steinhauser, M.; et al. Analytic next-to-leading order electroweak corrections to Higgs boson pair production at high energies. *arXiv* **2026**, arXiv:2603.08789.
29. Davies, J.; Schönwald, K.; Steinhauser, M.; et al. Next-to-leading order electroweak corrections to $gg \to HH$ and $gg \to gH$ in the large-m_t limit. *J. High Energy Phys.* **2023**, *10*, 033. https://doi.org/10.1007/JHEP10(2023)033.
30. Bi, H.Y.; Huang, L.H.; Huang, R.J.; et al. Electroweak corrections to double Higgs production at the LHC. *Phys. Rev. Lett.* **2024**, *132*, 231802. https://doi.org/10.1103/PhysRevLett.132.231802.
31. Bagnaschi, E.; Degrassi, G.; Gröber, R. Higgs boson pair production at NLO in the POWHEG approach and the top quark mass uncertainties. *Eur. Phys. J. C* **2023**, *83*, 1054. https://doi.org/10.1140/epjc/s10052-023-12238-8.
32. Mazzitelli, J. NNLO study of top-quark mass renormalization scheme uncertainties in Higgs boson production. *J. High Energy Phys.* **2022**, *9*, 065. https://doi.org/10.1007/JHEP09(2022)065.
33. ATLAS Collaboration. Search for non-resonant Higgs boson pair production in final states with leptons, taus, and photons in pp collisions at $\sqrt{s} = 13$ TeV with the ATLAS detector. *J. High Energy Phys.* **2024**, *8*, 164. https://doi.org/10.1007/JHEP08(2024)164.
34. ATLAS Collaboration. Combination of searches for Higgs boson pair production in pp collisions at $\sqrt{s} = 13$ TeV with the ATLAS detector. *Phys. Rev. Lett.* **2024**, *133*, 101801. https://doi.org/10.1103/PhysRevLett.133.101801.
35. CMS Collaboration. Combination of searches for nonresonant Higgs boson pair production in proton-proton collisions at $\sqrt{s} = 13$ TeV. *J. Phys. G* **2026**, *53*, 095001. https://doi.org/10.1088/1361-6471/ae8ff1.
36. ATLAS Collaboration. Search for Higgs boson pair production in the two bottom quarks plus two photons final state in pp collisions at $\sqrt{s} = 13$ TeV with the ATLAS detector. *Phys. Rev. D* **2022**, *106*, 052001. https://doi.org/10.1103/PhysRevD.106.052001.
37. ATLAS Collaboration. Studies of new Higgs boson interactions through nonresonant HH production in the $b\bar{b}\gamma\gamma$ final state in pp collisions at $\sqrt{s} = 13$ TeV with the ATLAS detector. *J. High Energy Phys.* **2024**, *1*, 066. https://doi.org/10.1007/JHEP01(2024)066.
38. CMS Collaboration. Search for nonresonant Higgs boson pair production in final states with two bottom quarks and two photons in proton-proton collisions at $\sqrt{s} = 13$ TeV. *J. High Energy Phys.* **2021**, *3*, 257. https://doi.org/10.1007/JHEP03(2021)257.

39. ATLAS Collaboration. Search for resonant and non-resonant Higgs boson pair production in the $b\bar{b}\tau^+\tau^-$ decay channel using 13 TeV pp collision data from the ATLAS detector. *J. High Energy Phys.* **2023**, *7*, 040. https://doi.org/10.1007/JHEP07(2023)040.
40. ATLAS Collaboration. Search for the non-resonant production of Higgs boson pairs via gluon fusion and vector-boson fusion in the $b\bar{b}\tau^+\tau^-$ final state in proton-proton collisions at $\sqrt{s} = 13$ TeV with the ATLAS detector. *Phys. Rev. D* **2024**, *110*, 032012. https://doi.org/10.1103/PhysRevD.110.032012.
41. CMS Collaboration. Search for nonresonant Higgs boson pair production in final state with two bottom quarks and two tau leptons in proton-proton collisions at $\sqrt{s} = 13$ TeV. *Phys. Lett. B* **2023**, *842*, 137531. https://doi.org/10.1016/j.physletb.2022.137531.
42. ATLAS Collaboration. Search for nonresonant pair production of Higgs bosons in the $b\bar{b}b\bar{b}$ final state in pp collisions at $\sqrt{s} = 13$ TeV with the ATLAS detector. *Phys. Rev. D* **2023**, *108*, 052003. https://doi.org/10.1103/PhysRevD.108.052003.
43. CMS Collaboration. Search for Higgs boson pair production in the four b quark final state in proton-proton collisions at $\sqrt{s} = 13$ TeV. *Phys. Rev. Lett.* **2022**, *129*, 081802. https://doi.org/10.1103/PhysRevLett.129.081802.
44. CMS Collaboration. Improved results on Higgs boson pair production in the 4b final state. *Phys. Rev. D* **2026**, *submitted*.
45. CMS Collaboration. Search for nonresonant pair production of highly energetic Higgs bosons decaying to bottom quarks. *Phys. Rev. Lett.* **2023**, *131*, 041803. https://doi.org/10.1103/PhysRevLett.131.041803.
46. ATLAS Collaboration. Search for pair production of boosted Higgs bosons via vector-boson fusion in the $b\bar{b}b\bar{b}$ final state using pp collisions at $\sqrt{s} = 13$ TeV with the ATLAS detector. *Phys. Lett. B* **2024**, *858*, 139007. https://doi.org/10.1016/j.physletb.2024.139007.
47. Elagin, A.; Murat, P.; Pranko, A.; et al. A New Mass Reconstruction Technique for Resonances Decaying to $\tau\tau$. *Nucl. Instrum. Methods Phys. Res. A* **2011**, *654*, 481–489. https://doi.org/10.1016/j.nima.2011.07.009.
48. Bianchini, L.; Conway, J.; Friis, E.K.; et al. Reconstruction of the Higgs mass in $H \to \tau\tau$ Events by Dynamical Likelihood Techniques. *J. Phys. Conf. Ser.* **2014**, *513*, 022035. https://doi.org/10.1088/1742-6596/513/2/022035.
49. CMS Collaboration. Search for Higgs boson pairs decaying to WW^*WW^*, $WW^*\tau\tau$, and $\tau\tau\tau\tau$ in proton-proton collisions at $\sqrt{s} = 13$ TeV. *J. High Energy Phys.* **2023**, *7*, 095. https://doi.org/10.1007/JHEP07(2023)095.
50. CMS Collaboration. Search for Higgs boson pair production in the $b\bar{b}W^+W^-$ decay mode in proton-proton collisions at $\sqrt{s} = 13$ TeV. *J. High Energy Phys.* **2024**, *7*, 293. https://doi.org/10.1007/JHEP07(2024)293.
51. ATLAS Collaboration. Search for non-resonant Higgs boson pair production in the $bb\ell\nu\ell\nu$ final state with the ATLAS detector in pp collisions at $\sqrt{s} = 13$ TeV. *Phys. Lett. B* **2020**, *801*, 135145. https://doi.org/10.1016/j.physletb.2019.135145.
52. Pierini, M. Precision physics in the era of (HL)LHC. *Highlights High Energy Phys.* **2025**, *1*, 11. https://doi.org/10.53941/hihep.2025.100011.
53. ATLAS Collaboration. ATLAS flavour-tagging algorithms for the LHC Run 2 pp collision dataset. *Eur. Phys. J. C* **2023**, *83*, 681. https://doi.org/10.1140/epjc/s10052-023-11699-1.
54. Bols, E.; Kieseler, J.; Verzetti, M.; et al. Jet flavour classification using DeepJet. *J. Instrum.* **2020**, *15*, P12012. https://doi.org/10.1088/1748-0221/15/12/P12012.
55. ATLAS Collaboration. Transforming jet flavour tagging at ATLAS. *Nat. Commun.* **2026**, *17*, 541. https://doi.org/10.1038/s41467-025-65059-6.
56. Qu, H.; Gouskos, L. ParticleNet: jet tagging via particle clouds. *Phys. Rev. D* **2020**, *101*, 056019. https://doi.org/10.1103/PhysRevD.101.056019.
57. Qu, H.; Li, C.; Qian, S. Particle Transformer for Jet Tagging. In Proceedings of the 39th International Conference on Machine Learning, Baltimore, MD, USA, 17–23 July 2022; Volume 162, pp. 18281–18292.
58. CMS Collaboration. *Flavour Tagging Performance of the Updated Unified Particle Transformer Algorithm with the CMS Experiment at $\sqrt{s} = 13.6$ TeV*; Technical Report CMS-DP-2025-081; CERN: Geneva, Switzerland, 2025.
59. ATLAS Collaboration. *GN3: Multi-Task, Multi-Modal Transformers for Jet Flavour Tagging in ATLAS*; Technical Report ATL-PHYS-PUB-2026-001; CERN: Geneva, Switzerland, 2026.
60. ATLAS Collaboration. *Carpe Datum: Scaling Behavior of Transformers for Heavy Hadron Flavor Identification*; Technical Report ATL-SOFT-PUB-2026-002; CERN: Geneva, Switzerland, 2026.
61. ATLAS Collaboration. Study of Higgs boson pair production in the $HH \to b\bar{b}\gamma\gamma$ final state with 308 fb^{-1} of data collected at $\sqrt{s} = 13$ TeV and 13.6 TeV by the ATLAS experiment. *Phys. Lett. B* **2026**, *876*, 140280. https://doi.org/10.1016/j.physletb.2026.140280.
62. CMS Collaboration. Search for the standard model Higgs boson produced in association with a W or a Z boson and decaying to bottom quarks. *Phys. Rev. D* **2014**, *89*, 012003. https://doi.org/10.1103/PhysRevD.89.012003.
63. CMS Collaboration. A deep neural network for simultaneous estimation of b jet energy and resolution. *Comput. Softw. Big Sci.* **2020**, *4*, 10. https://doi.org/10.1007/s41781-020-00041-z.
64. ATLAS Collaboration. Evidence for the $H \to b\bar{b}$ decay with the ATLAS detector. *J. High Energy Phys.* **2017**, *12*, 024. https://doi.org/10.1007/JHEP12(2017)024.
65. ATLAS Collaboration. *Transformer Networks for Constituent-Based b-Jet Calibration with the ATLAS Detector*; Technical Report ATL-PHYS-PUB-2024-015; CERN: Geneva, Switzerland, 2024.

66. ATLAS Collaboration. *Identification of Boosted Higgs Bosons Decaying into a Pair of Collimated τ-Leptons Decaying Hadronically with Transformer Neural Networks in ATLAS*; ATLAS PUB Note ATL-PHYS-PUB-2025-026; CERN: Geneva, Switzerland, 2025.
67. CMS Collaboration. *Performance of Boosted Tau Lepton Identification with DeepTau Framework (Boosted DeepTau)*; CMS Detector Performance Summary CMS-DP-2025-047; CERN: Geneva, Switzerland, 2025.
68. ATLAS Collaboration. Reconstruction and identification of boosted di-τ systems in a search for Higgs boson pairs using 13 TeV proton-proton collision data in ATLAS. *J. High Energy Phys.* **2020**, *11*, 163. https://doi.org/10.1007/JHEP11(2020)163.
69. ATLAS Collaboration. Configuration, performance, and commissioning of the ATLAS b-jet triggers for the 2022 and 2023 LHC data-taking periods. *J. Instrum.* **2025**, *20*, P03002. https://doi.org/10.1088/1748-0221/20/03/P03002.
70. CMS Collaboration. Enriching the physics program of the CMS experiment via data scouting and data parking. *Phys. Rep.* **2025**, *1115*, 678–772. https://doi.org/10.1016/j.physrep.2024.09.006.
71. CMS Collaboration. High-level hadronic tau lepton triggers of the CMS experiment in proton-proton collisions at $\sqrt{s} = 13.6$ TeV. *J. Instrum.* **2026**, *21*, P04002. https://doi.org/10.1088/1748-0221/21/04/P04002.
72. CMS Collaboration. *Performance of Hadronic Tau Reconstruction at the High Level Trigger Using 2024 Data from the CMS Experiment at CERN*; CMS Detector Performance Summary CMS-DP-2026-008; CERN: Geneva, Switzerland, 2026.
73. CMS Collaboration. *Search for Nonresonant Higgs Boson Pair Production in the $b\bar{b}\tau^+\tau^-$ Final State in Proton-Proton Collisions at $\sqrt{s} = 13.6$ TeV*; CMS Physics Analysis Summary CMS-PAS-HIG-25-008; Preliminary; CERN: Geneva, Switzerland, 2026.
74. CMS Collaboration. Search for resonant pair production of Higgs bosons decaying to two bottom quark-antiquark pairs in proton-proton collisions at 8 TeV. *Phys. Lett. B* **2015**, *749*, 560. https://doi.org/10.1016/j.physletb.2015.08.047.
75. ATLAS Collaboration. Improved analysis of non-resonant Higgs boson pair production in the $b\bar{b}\tau^+\tau^-$ final state with 196 fb^{-1} of data collected at $\sqrt{s} = 13$ TeV and 13.6 TeV with the ATLAS detector. *Eur. Phys. J. C* **2026**, *submitted*.
76. CMS Collaboration. *A Search for $HH \to b\bar{b}\gamma\gamma$ Production in Proton-Proton Collisions at $\sqrt{s} = 13.6$ TeV with a Partial CMS Run 3 Dataset*; CMS Physics Analysis Summary CMS-PAS-HIG-25-007; CERN: Geneva, Switzerland, 2026.
77. CMS Collaboration. Search for Higgs boson pair production in the $b\bar{b}WW$ decay channel with two leptons in the final state using proton-proton collision data at $\sqrt{s} = 13.6$ TeV. *J. High Energy Phys.* **2026**, *8*, 019. https://doi.org/10.1007/JHEP08(2026)019.
78. ATLAS Collaboration. Search for Higgs boson pair production in association with a vector boson in pp collisions at $\sqrt{s} = 13$ TeV with the ATLAS detector. *Eur. Phys. J. C* **2023**, *83*, 519. https://doi.org/10.1140/epjc/s10052-023-11559-y.
79. CMS Collaboration. Search for Higgs boson pair production with one associated vector boson in proton-proton collisions at $\sqrt{s} = 13$ TeV. *J. High Energy Phys.* **2024**, *10*, 061. https://doi.org/10.1007/JHEP10(2024)061.
80. ATLAS Collaboration. Search for Higgs boson pair production in association with top-quark pairs using 196 fb^{-1} of proton-proton collision data at $\sqrt{s} = 13$ and 13.6 TeV with the ATLAS detector. *J. High Energy Phys.* **2026**, *8*, 020. https://doi.org/10.1007/JHEP08(2026)020.
81. CMS Collaboration. *Search for Nonresonant $t\bar{t}HH$ Production in the Final State with Four Bottom Quarks and One Lepton in Proton-Proton Collisions at $\sqrt{s} = 13$ TeV*; CMS Physics Analysis Summary CMS-PAS-HIG-24-016; Preliminary; CERN: Geneva, Switzerland, 2026.
82. Lang, J. Precise SMEFT predictions for di-Higgs production. In Proceedings of the Eleventh Annual Conference on Large Hadron Collider Physics (LHCP2023), Belgrade, Serbia, 22–26 May 2023; Volume 450. https://doi.org/10.22323/1.450.0192.
83. Heinrich, G.; Lang, J. Combining chromomagnetic and four-fermion operators with leading SMEFT operators for $gg \to hh$ at NLO QCD. *J. High Energy Phys.* **2024**, *5*, 121. https://doi.org/10.1007/JHEP05(2024)121.
84. Heinrich, G.; Lang, J. Renormalisation group effects in SMEFT for di-Higgs production. *SciPost Phys.* **2025**, *18*, 113. https://doi.org/10.21468/SciPostPhys.18.3.113.
85. Di Noi, S.; Gröber, R.; Heinrich, G.; et al. Subleading operators and γ_5-scheme dependence in SMEFT for Higgs boson pair production. In Proceedings of the Conference of Loops and Legs in Quantum Field Theory (LL2024), Wittenberg, Germany, 14–19 April 2024; Volume 467. https://doi.org/10.22323/1.467.0021.
86. Asiáin, Í.; Gröber, R.; Tiberi, L. Is the Standard Model effective field theory enough for Higgs pair production? *arXiv* **2026**, arXiv:2602.16288.
87. ATLAS Collaboration. *Effective Field Theory Interpretations of the Search for $HH \to b\bar{b}\gamma\gamma$ with 308 fb^{-1} of Data Collected at $\sqrt{s} = 13$ TeV and 13.6 TeV with the ATLAS Detector*; ATLAS PUB Note ATL-PHYS-PUB-2025-034; CERN: Geneva, Switzerland, 2025.
88. ATLAS Collaboration. Constraints on the Higgs boson self-coupling from single- and double-Higgs production with the ATLAS detector using pp collisions at $\sqrt{s} = 13$ TeV. *Phys. Lett. B* **2023**, *843*, 137745. https://doi.org/10.1016/j.physletb.2023.137745.
89. CMS Collaboration. Constraints on the Higgs boson self-coupling from the combination of single and double Higgs boson production in proton-proton collisions at $\sqrt{s} = 13$ TeV. *Phys. Lett. B* **2025**, *861*, 139210. https://doi.org/10.1016/j.physletb.2024.139210.
90. ter Hoeve, J.; Mantani, L.; Rojo, J.; et al. Higgs trilinear coupling in the Standard Model effective field theory at the high luminosity LHC and the FCC-ee. *Phys. Rev. D* **2025**, *112*, 013008. https://doi.org/10.1103/qtz8-bkd4.

91. Cepeda, M.; Gori, S.; Ilten, P.; et al. (Eds.) Report from Working Group 2: Higgs Physics at the HL-LHC and HE-LHC. In *CERN Yellow Reports: Monographs*; CERN: Geneva, Switzerland, 2019; Volume 7, pp. 221–584. https://doi.org/10.23731/CYRM-2019-007.221.
92. ATLAS Collaboration; CMS Collaboration. Highlights of the HL-LHC physics projections by ATLAS and CMS. *arXiv* **2025**, arXiv:2504.00672.
93. Huang, P.; Joglekar, A.; Li, B.; et al. Probing the Electroweak Phase Transition at the LHC. *Phys. Rev. D* **2016**, *93*, 055049. https://doi.org/10.1103/PhysRevD.93.055049.
94. FCC Collaboration. Future Circular Collider Feasibility Study Report: Volume 1, Physics, Experiments, Detectors. *Eur. Phys. J. C* **2025**, *85*, 1468. https://doi.org/10.1140/epjc/s10052-025-15077-x. Erratum in *Eur. Phys. J. C* **2026**, *86*, 844.
95. Abramowicz, H.; Adli, E.; Alharthi, F.; et al. A Linear Collider Vision for the Future of Particle Physics. *Eur. Phys. J. Spec. Top.* **2026**, *235*, 1641–1796. https://doi.org/10.1140/epjs/s11734-026-02153-w.
96. Berggren, M.; Bliewert, B.; List, J.; et al. Update of the Higgs self-coupling projections from di-Higgs production in detailed simulation of the ILD concept. *arXiv* **2025**, arXiv:2509.14148.